frontiers in Nanotechnology

ORIGINAL RESEARCH
published: 20 April 2021
doi: 10.3389/fnano.2021.644734

The Effect of Surface Coating of Iron Oxide Nanoparticles on Magnetic Resonance Imaging Relaxivity

*Fatemeh Ahmadpoor[1], Atif Masood[2], Neus Feliu[3,4], Wolfgang J. Parak[4] and Seyed Abbas Shojaosadati[5]**

[1]Department of Materials Engineering, Tarbiat Modares University, Tehran, Iran, [2]Karachi Institute of Radiotherapy and Nuclear Medicine, Karachi, Pakistan, [3]The Fraunhofer Center for Applied Nanotechnology (CAN), Hamburg, Germany, [4]Fachbereich Physik and CHyN, Universität Hamburg, Hamburg, Germany, [5]Biotechnology Group, Faculty of Chemical Engineering, Tarbiat Modares University, Tehran, Iran

Iron oxide nanoparticles (IONPs) with acceptable biocompatibility and size-dependent magnetic properties can be used as efficient contrast agents in magnetic resonance imaging (MRI). Herein, we have investigated the impact of particle size and surface coating on the proton relaxivity of IONPs, as well as engineering of small IONPs' surface coating as a strategy for achieving gadolinium-free contrast agents. Accordingly, polymer coating using poly(isobutylene-alt-maleic anhydride) (PMA) with overcoating of the original ligands was applied for providing colloidal stability to originally oleic acid–capped IONPs in aqueous solution. In case of replacement of the original ligand shell, the polymer had been modified with dopamine. Furthermore, the colloidal stability of the polymer-coated IONPs was evaluated in NaCl and bovine serum albumin (BSA) solutions. The results indicate that the polymer-coated IONPs which involved replacement of the original ligands exhibited considerably better colloidal stability and higher proton relaxivity in comparison to polymer-coated IONPs with maintained ligand shell. The highest r_2/r_1 we obtained was around 300.

Keywords: iron oxide nanoparticles, polymer coating, surface engineering, proton relaxivity, colloidal stability

OPEN ACCESS

Edited by:
Yogendra Kumar Mishra, University of Southern Denmark, Denmark

Reviewed by:
Ajeet Kaushik, Florida Polytechnic University, United States
Suresh K. Verma, KIIT University, India

****Correspondence:***
Seyed Abbas Shojaosadati
shoja_sa@modares.ac.ir

Specialty section:
This article was submitted to Biomedical Nanotechnology, a section of the journal Frontiers in Nanotechnology

Received: *21 December 2020*
Accepted: *09 February 2021*
Published: *20 April 2021*

Citation:
Ahmadpoor F, Masood A, Feliu N, Parak WJ and Shojaosadati SA (2021) The Effect of Surface Coating of Iron Oxide Nanoparticles on Magnetic Resonance Imaging Relaxivity. Front. Nanotechnol. 3:644734. doi: 10.3389/fnano.2021.644734

INTRODUCTION

Magnetic iron oxide nanoparticles (IONPs) exhibit unique magnetic properties that make them attractive for different biomedical applications, including drug delivery (Karimi et al., 2016), magnetic resonance imaging (MRI) (Bruns et al., 2009; Kudr et al., 2017; Li et al., 2017; Smith and Gambhir, 2017; Woodard et al., 2018), magnetic particle imaging (Bauer et al., 2015), and magnetic hyperthermia (Laurent et al., 2011; Pardo et al., 2020). The magnetic properties of IONPs are influenced by the particle size, which arise from the magnetic domain structure (Tromsdorf et al., 2007; Li et al., 2017). Superparamagnetic iron oxide nanoparticles (SPIONs) are single-domain IONPs with a diameter of a few to a few tens nanometers that exhibit no remanent magnetization in the absence of an external magnetic field at room temperature. The superparamagnetic property of SPIONs, as well as their relatively good biocompatibility (Heine et al., 2014; Sheel et al., 2020), makes them the currently most used iron oxide–based T_2 contrast agents (Kwon et al., 2018). Generally, large SPIONs provide T_2 contrast due to the magnetic inhomogeneity induced by their strong magnetic moment. However, SPIONs-based T_2 contrast agents generate dark signal in T_2-weighted MRI that can mislead the clinical diagnosis (Zhao et al., 2013; Fernández-Barahona et al., 2020). In

this respect, T_1 contrast agents are more desirable for high accurate resolution imaging (Wei et al., 2017; Li et al., 2019). T_1 contrast agents are commonly based on paramagnetic compounds with a large number of unpaired electrons. This includes, for example, Gd^{3+} and Mn^{2+}(Ni et al., 2017). T_1 contrast is induced by magnetic coupling interaction between the nucleic spins of the protons of water molecules and the electron spins of the contrast agents. Gadolinium complexes are widely used as T_1 contrast agents, despite the fact that free gadolinium ions, leached from gadolinium complexes, have shown a long-term toxicity including nephrogenic systemic fibrosis and Gd deposition in the brain (Khawaja et al., 2015; McDonald et al., 2015). Because of these limitations, development of alternatives may help to overcome the drawbacks of Gd-based T_1 contrast agents.

Some groups have suggested that the long-term biocompatibility of iron compared with gadolinium makes IONPs very attractive materials for T_1 contrast agents (Tromsdorf et al., 2009; Shen et al., 2017). The magnetic moment of IONPs rapidly decreases as their sizes decrease due to the reduction in volume magnetic anisotropy and spin canting effect (Morales et al., 1997; Jun et al., 2008). Since the paramagnetic properties of small IONPs are similar to Gd-based contrast agents, these nanoparticles can be utilized as T_1 contrast agents because of small magnetic moment and low toxicity (Bao et al., 2018). It however has to be pointed out that also for IONPs toxic effects exist (Joris et al., 2017; Feng et al., 2018; Patil et al., 2018), though to a much lesser extent than for chelated Gd. Toxicity may depend on various physicochemical properties such as size, shape, structure, concentration, surface modification, and solubility (Vanhecke et al., 2017; Feng et al., 2018; Patil et al., 2018; Vakili-Ghartavol et al., 2020).

MRI contrast enhancement arises from the signal difference between water molecules residing in different environments that are under the effect of magnetic nanoparticles (NPs). The size of IONPs and their surface properties (thickness and chemical composition) (Wang et al., 2017), as also doping (Pardo et al., 2020), have influence on the contrast enhancement of SPIONs (Zhang et al., 2018). Consequently, understanding the relationships between the relaxivities of water protons under influence of magnetic NPs and intrinsic properties of these NPs can give decisive information for predicting the properties of engineered magnetic NPs. This may help enhancing their performance in MRI-based theranostic applications (Huang et al., 2012). Duan et al., for example, reported that the hydrophilic nature of the surface coating contributes to the relaxivity of MRI contrast agent (Duan et al., 2008).

Hydrophobic IONPs that are synthesized in organic solvents can exhibit improved sized distribution, crystallinity, and magnetic properties in comparison to iron oxide nanoparticles by aqueous phase methods (Lee and Hyeon, 2012; Wu et al., 2015). However, the effect of the coating and the ligand density on the T_1 and T_2 relaxation times is not fully understood yet.

The aim of this work is to prepare SPIONs stabilized with polymer by overcoating and replacement of the original ligand shell methods, in order to elucidate the influence of the polymer type and polymer coating on the corresponding longitudinal (r_1) and transverse (r_2) relaxivities.

MATERIALS AND METHODS

Materials. Oleic acid (OA, ≥93% technical grade), dopamine hydrochloride, poly(isobutylene-alt-maleic anhydride) (PMA) (average Mw: 6,000 Da), triethylamine, oleylamine, 1,2 hexadecanediol, benzyl ether, 1-octadecne, trioctylamine, dodecylamine dimethylformamide (DMF), and anhydrous sodium sulfate and iron (III) acetylacetonate were provided by Sigma. Ethanol (EtOH >96%), toluene (≥95% Sigma), and chloroform were obtained from Carl Roth. Poly(ethylene glycol) methyl ether (PEG, average Mw: 750 Da) was from Rapp Polymer. $FeCl_3{\cdot}6H_2O$ and sodium oleate were purchased from Merck and TCI, respectively.

Column chromatography was performed using silica gel (60 Å) acquired from Fluka. The chemicals and solvents were used as received, unless otherwise specified. All the syntheses were carried out under N_2 atmosphere using MBraun LABmaster glovebox and standard Schlenk techniques.

Synthesis of Iron Oxide Nanoparticles

Iron Oxide Nanoparticles of 15 nm to 18 nm. IONPs were synthesized by thermal decomposition according to the method described by Hyeon and coworkers with minor modifications (Park et al., 2004). Briefly, to synthesize the iron oleate precursor, a 100 ml flask equipped with a Teflon-coated magnetic stir bar, 9.13 g sodium oleate (30 mmol), and hexane (3 ml) was added. The mixture was stirred, and then ethanol (20 ml) was added. All the solids dissolved by slow addition of distilled water (7.5 ml) according to the previously published protocol (Park et al., 2004). The reaction was heated to 40°C with stirring. At this point, the sodium oleate was completely dissolved. Then, a solution of 2.7 g of iron chloride ($FeCl_3{\cdot}6H_2O$, 10 mmol) in 7.5 ml water was added to the reaction vessel. The resulting solution was heated under gentle reflux (65–70°C) and was kept at that temperature for 4 h. When the reaction was completed, the solution was transferred to a separation funnel. The upper red layer was washed with water and transferred to an Erlenmeyer flask containing anhydrous sodium sulfate (3 g) in order to remove residual water. Then, the solution was swirled and filtered with a hydrophobic filter (0.2 μm, Millipore #SLFG025N). The solution was concentrated on a rotary evaporator. After drying in high vacuum, the resulting product was a reddish brown viscous oil with a mass of around 9 g.

The synthesis of the IONPs relies on the reduction of iron oleate at high temperature. In a typical experiment, IONPs with a core diameter of 15 nm were prepared as follows: 3.6 g (4 mmol) of iron oleate and 0.57 g oleic acid were dissolved in 20 ml of 1-octadecene, in a three-neck round-bottom reaction flask attached to the Schlenk line. Next, the mixture was degassed and dried through heating at 100°C for 45 min, in order to remove volatile impurities and remaining traces of water in the iron oleate precursor. The mixture was afterward heated to 320°C at a heating rate of around 3.3°C/min and was kept for 30 min under an inert atmosphere. A severe reaction occurred when the reaction temperature reached 320°C, and the initially transparent solution became turbid and brownish black. The

18 nm IONPs were obtained by thermal decomposition of iron oleate in the presence of oleic acid (0.57 g) in trioctylamine (20 ml) at 360°C for 30 min. The resulting solution was allowed to cool down to room temperature by removing the heating mantle, and then, acetone was added to the solution to precipitate the IONPs. The IONPs were precipitated by centrifugation (3,500 rpm, 5 min). The supernatant was discarded, and the IONP precipitate was dispersed in toluene. The concentration of the IONPs in solution (i.e., toluene) was estimated by weighing and determining the mass of one IONP by transmission electron microscopy (TEM) analysis (Hühn et al., 2016). In the following, the concentration of IONPs was calculated by assuming that they are Fe_3O_4 spheres of 18 nm core diameter (d_c = 18 nm). The volume of one IONP is $V_{NP} = (4/3) \times \pi \times (d_c/2)^3 = (4/3) \times \pi \times [(18 \times 10^{-7}\ cm)/2]^3 = 3{,}050 \times 10^{-21}\ cm^3$. The density of the IONP cores was assumed as the bulk density of Fe_3O_4 which is 5.18 g/cm^3 (Kurzhals et al., 2017; Patsula et al., 2019). Therefore, the mass of each IONP is $m_{NP} = \rho_{NP} \times V_{NP} = (5.18\ g/cm^3) \times (3{,}050 \times 10^{-21}\ cm^3) = 15{,}800 \times 10^{-21}$ g. The number of IONPs (N_{NP}) in solution of volume $V_{solution}$ can be determined by dividing the total mass of dried IONPs ($m_{NP,tot}$) originating for a solution of $V_{solution}$ = 1 ml by the mass of single nanoparticle $N_{NP} = (m_{NP,tot}/m_{NP}) = (30 \times 10^{-3}\ g)/(15{,}800 \times 10^{-21}\ g) = 0.0019 \times 10^{18}$. The concentration of sample is then $C_{NP} = (N_{NP}/N_A)/V_{solution} = [(0.0019 \times 10^{18})/(6.022 \times 10^{23})]/(1 \times 10^{-3}\ L) = 3.15\ \mu M$ with Avogadro's constant $N_A = 6.022 \times 10^{23}\ mol^{-1}$.

Iron Oxide Nanoparticles of 6 nm. IONPs with a core diameter of around 6 nm were synthesized via the procedure reported by Sun et al. (Sun et al., 2004). Fe $(acac)_3$ (2 mmol), oleic acid (6 mmol), benzyl ether (20 ml), oleylamine (6 mmol), and 1,2-hexadecanediol (10 mmol) were mixed and magnetically stirred under a flow of nitrogen. The mixture was heated to 200°C for 2 h and then was refluxed (~300°C) for 1 h under nitrogen atmosphere. A black-brown hexane dispersion of 6 nm IONPs was produced. After that, the heating was switched off and the black-brown mixture was allowed to cool to room temperature. Finally, the product was precipitated with ethanol (40 ml) and collected by centrifugation (5,000 rpm, 10 min). Then, IONPs were redispered in a mixture of hexane with 1% (v/v) oleic acid and oleylamine.

We note that, in the present work, synthesis was reproduced from previous publications, in which key characterization of these IONPs is also provided (Park et al., 2004; Sun et al., 2004). The Fe_3O_4 structure of the IONPs has not been explicitly verified in the present work, though there are different methods for this (Komadel and Stucki, 1988; Corrias et al., 2009), but it is based on the findings in the original reports about the syntheses. Some additional basic characterization (XRD, FTIR, and VSM) is provided in the Supporting Information.

Polymer Coating

Polymer Coating Involving Overcoating of the Original Ligand Shell. The IONPs were transferred into aqueous solution with overcoating them using the polymer dodecylamine–modified poly(isobutylene-alt-maleic anhydride) as described previously (Hühn et al., 2016). The amphiphilic polymer comprises a backbone of poly(isobutylene-alt-maleic anhydride), and hydrophobic side chains in the form of dodecylamine were linked to the anhydride rings through formation of amide bonds. In the amphiphilic polymer PMA–DDA used in the present work, 75% of its maleic anhydride rings had been reacted with dodecylamine and 25% of its anhydride rings were left unreacted (Hühn et al., 2016). The leftover anhydride rings of the hydrophilic backbone open up under alkaline conditions, yielding negatively charged carboxylic groups that make the IONPs soluble in aqueous solutions. Briefly, polymer coating of the IONPs was performed by dissolving a desirable amount of polymer monomers per surface area of IONP. In all of the samples, we added 3,000 monomers of poly(isobutylene-alt-maleic anhydride) modified with dodecylamine (PMA–DDA) dissolved in chloroform per 1 nm^2 of effective surface area of the IONPs (Yang et al., 2017). The concentrations of the IONPs CNP samples were calculated (Hühn et al., 2016) as described above. Then, the volume of polymer solution (V_p) for efficient polymer coating of the IONPs was determined as described in previous work (Hühn et al., 2013; Hühn et al., 2016; Zhu et al., 2019):

$$V_p = \frac{R_{\frac{p}{area}} \times \pi \times d_{eff}^2 \times C_{NP} \times V_{NP}}{C_p}, \quad (1)$$

where C_p and R_p/area are the monomer concentration and the ratio of polymer units per nm^2 of effective surface area, respectively (Hühn et al., 2016). CNP and VNP are the concentration and the volume of the IONP solution. The effective diameter of IONPs (d_{eff}) includes the diameter of the iron oxide cores from TEM images and twice the hydrophobic stabilizing ligand shell: $d_{eff} = d_c + 2d_{ligand}$ and we assumed d_{ligand} = 1 nm. Here, we mixed IONPs with C_p = 0.05 M monomer concentration and R_p/area = 100 nm^{-2}. After addition of the polymer in a round flask, the solvent was slowly removed using a low-pressure system under heating to 40°C in order to force the polymer to wrap around the IONPs. Then, again chloroform was added and the drying process was repeated. The IONP powder was then dissolved in sodium borate buffer at pH 12. Here, hydrolysis of the remaining maleic anhydride left two carboxylic groups per newly opened anhydride ring. Then, the solution was filtered using a 0.22 μm syringe filter. Afterward, the IONPs were precipitated by centrifugation and the supernatant was discarded, and the IONPs were redispersed in Milli-Q water. This procedure was repeated in order to remove residual empty polymer micelles (Fernández-Argüelles et al., 2007). After purification, the IONPs were redispersed and kept in Milli-Q water.

Polymer Coating Involving Replacement of the Original Ligand Shell. The polymer coating was carried out by following a previously reported procedure (Wang et al., 2014). Briefly, to achieve dopamine functionalized PMA, the polymer synthesis was carried out by dissolving 0.385 g of PMA in 10 ml of DMF in a 50 ml three-necked round bottom flask. The solution was purged with nitrogen, and then, the temperature was raised to 70°C. Then, a mixture of amino–PEG (H_2N–PEG–OMe, 0.995 g) and dopamine hydrochloride (0.237 g) activated with triethylamine (resulting in free amine dopamine) was added dropwise to the solution, and the mixture was left to react

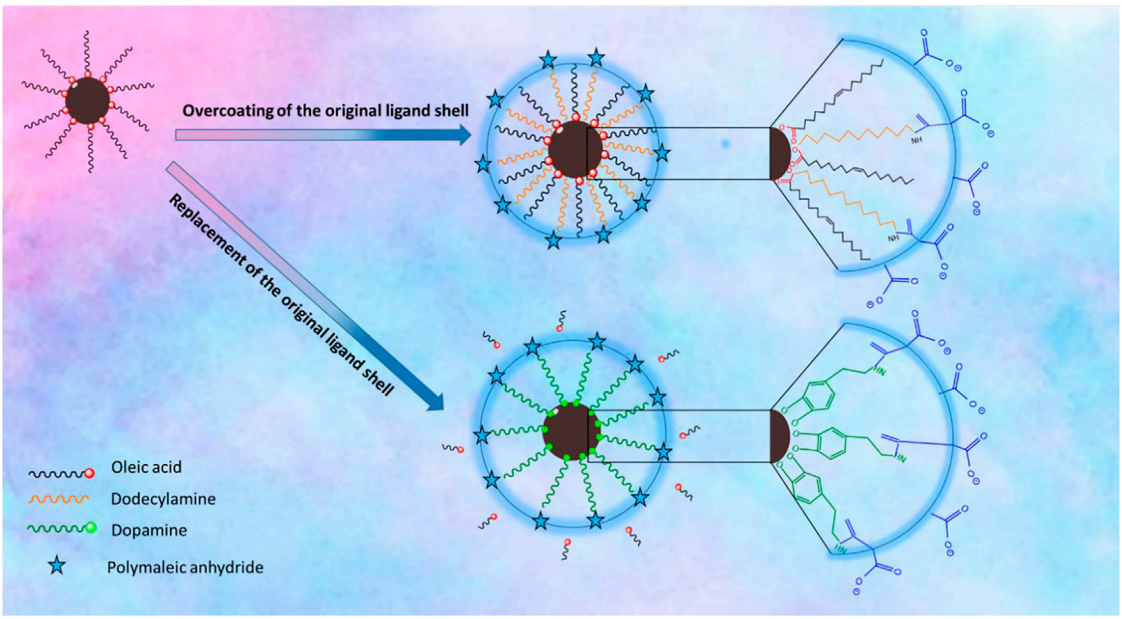

FIGURE 1 | Schematic illustration of the surface chemistry of the IONPs via overcoating of the original ligand shell which relies on coating of the native hydrophobic IONPs with an amphiphilic polymer PMA–DDA; replacement of the original ligand shell involves the removal of the original ligand and replacing it with dopamine-functionalized PMA.

overnight at 70°C. To collect the polymer, DMF was removed under vacuum and then dissolved in chloroform. The solution was purified by silica gel column chromatography and eluted with chloroform. Afterward, the solvent evaporated and a gel-like yellow oil was collected as the resultant product. The polymer coating was carried out as follows: First, 5 mg of precipitated IONPs was dispersed in 0.5 ml THF. To this mixture, 1 ml of THF containing 0.25 mg of dopamine–PMA–PEG was added. Subsequently, the mixture was sealed and stirred overnight at 50°C under nitrogen atmosphere. Then, an excess of hexane was added to precipitate the sample and was centrifuged. The supernatant was discarded and the precipitate was dried. The final black pellet was dispersed easily in Milli-Q water by sonication. The aqueous solution was filtered with a 0.22 µm syringe filter, and the IONPs were precipitated by centrifugation. Unbound excess ligands were discarded with the supernatant and the IONPS were redispersed and kept in Milli-Q water. Both coating procedures are summarized in **Figure 1**.

Characterization of Iron Oxide Nanoparticles

All samples were characterized by dynamic light scattering (DLS; Nanosizer, Malvern) and inductively coupled plasma mass spectroscopy (ICP-MS; Agilent 7700 series ICP-MS). The morphology and size distribution of the IONPs were examined with a transmission electron microscope (TEM, JEOL 1400 plus 100 kV and LEO 912 AB, 120 kV). TEM samples were prepared by dropping a dilute solution of IONPs on carbon-coated copper grids and letting the solvent evaporate. The thickness of the organic shell was determined by TEM with uranyl acetate negative staining (Yang et al., 2017). Gel electrophoresis analysis was performed on a Bio-Rad system using 2% agarose gel. Electrophoresis was carried out for 60 min at 100 V.

Relaxivity Measurements. The magnetic resonance (MR) relaxivity profile was evaluated in phantoms and the solutions of the IONPs at different concentrations (c_{Fe} = 0.035, 0.07, 0.14, 0.28, and 0.56 mM equivalent Fe content) by using a MRI scanner with 3 T field strength (Siemens). The longitudinal relaxation times (T_1) were determined using an inversion recovery pulse sequence (repetition time (T_R) = 100, 200, 500, 750 and 1,000 ms and fixed echo time (T_E) = 12 ms. The T_1 relaxation time of each sample was determined based on the equation $I \sim M_0 (1 - 2 \cdot \exp(-t/T_1)$ to fit the magnitude of the MRI signals at different inversion times.

A multiple spin echo was used to simultaneously collect data points at different echo times (T_E = 6–180 ms with an increment of 6 ms) for the T_2 measurements. A nonlinear monoexponential equation $I \sim M_0 \cdot \exp(-T_E/T_2)$ was used to determine the T_2 relaxation time of each IONP sample (Ahmad et al., 2011). Finally, r_1 and r_2 values were calculated according to the linear relationship of longitudinal and transverse relaxation rates vs. iron concentration of IONPs (Hobson et al., 2019; Ahmadpoor et al., 2020).

RESULTS

Iron Oxide Nanoparticles Synthesis and Polymer Coating

IONPs can be prepared by aqueous and nonaqueous methods. Aqueous methods such as coprecipitation usually produce IONPs

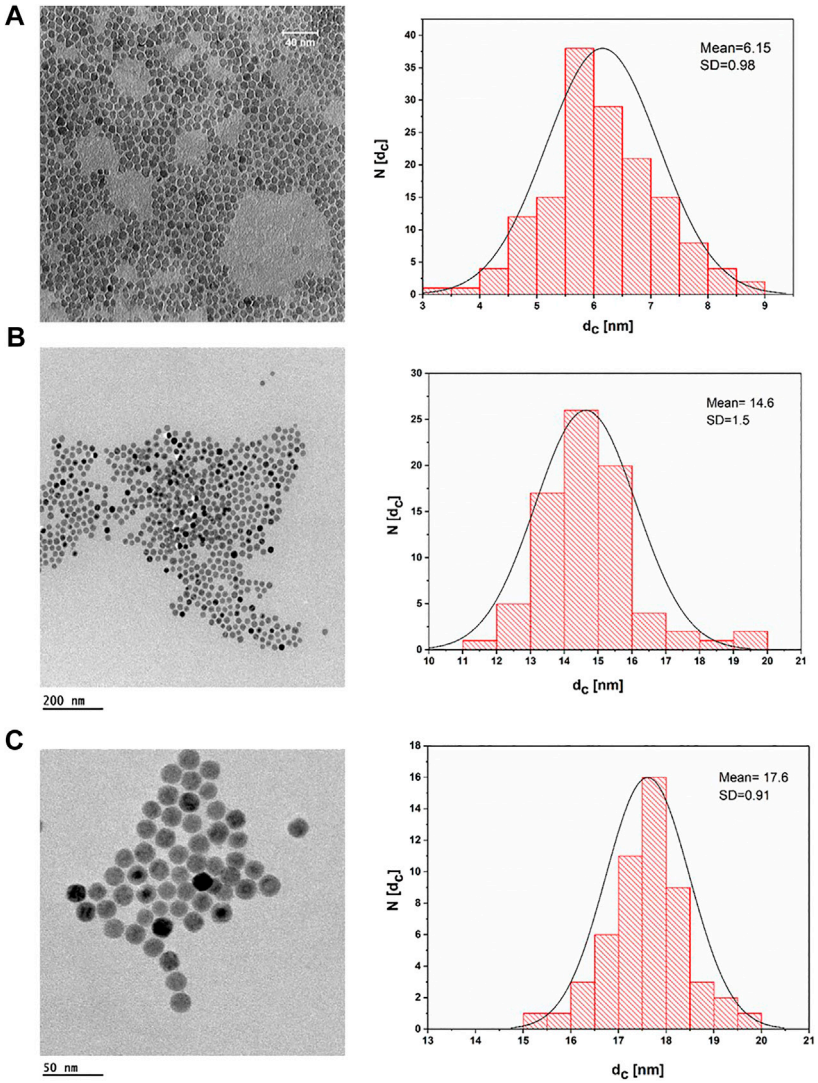

FIGURE 2 | TEM bright field images of IONPs dried on a grid from a suspension of IONPs in hexane and their corresponding histogram, plotted as the number of NPs (N) that have a core diameter of d_c. **(A)** IONPs with d_c = (6.5 ± 0.98) nm; the scale bar corresponds to 40 nm. **(B)** IONPs with d_c = (14.6 ± 1.5) nm; the scale bar corresponds to 200 nm. **(C)** IONPs with d_c = (17.6 ± 0.91) nm; the scale bar corresponds to 50 nm.

with low crystallinity and a broad size distribution (Ali et al., 2016). In contrast, nonaqueous methods such as thermal decomposition may generate better monodispersed IONPs with high crystallinity. In the present work, three different sizes of IONPs capped with oleic acid were synthesized by the thermal decomposition method. For this purpose, a modified protocol of the previously reported procedure was used. **Figure 2** depicts TEM images of the uniform spherical IONPs, which demonstrate a narrow size distribution. The inorganic (core) diameter of the IONPs (d_c) was derived from the TEM images using the software Image J, resulting in core diameters d_c of the three different samples of 6.15 ± 0.98, 14.6 ± 1.5, and 17.6 ± 0.91 nm.

The XRD pattern of IONPs (6 nm) (**Supplementary Figure SI-1**) demonstrates sharp diffraction peaks that are consistent with the magnetite phase (JCPDF #19–0629). Also, the FTIR spectra of IONPs (**Supplementary Figure SI-3**) show the strong characteristic band at 574 cm^{-1} with a shoulder at 630 cm^{-1}, which are related to the vibrations of Fe–O from octahedral and tetrahedral sites of magnetite (Muthukumaran and Philip, 2016). The peaks from 1,408 to 1,586 cm^{-1} are due to the vibrations of COO from adsorbed oleic acid over magnetite. The peaks at 2,874 and 2,915 cm^{-1} are assigned to the stretching modes of CH_2 and CH_3 groups of oleic acid (Li et al., 2010). **Supplementary Figure SI-2** shows the magnetic behavior of IONPs at room temperature. The saturation magnetization value obtained from the M-H curve under an applied magnetic field of 80 kOe is about 35 emu/g, and the IONPs exhibit superparamagnetic properties.

Two strategies have been applied for surface modification of hydrophobic magnetic IONPs to render them colloidally stable

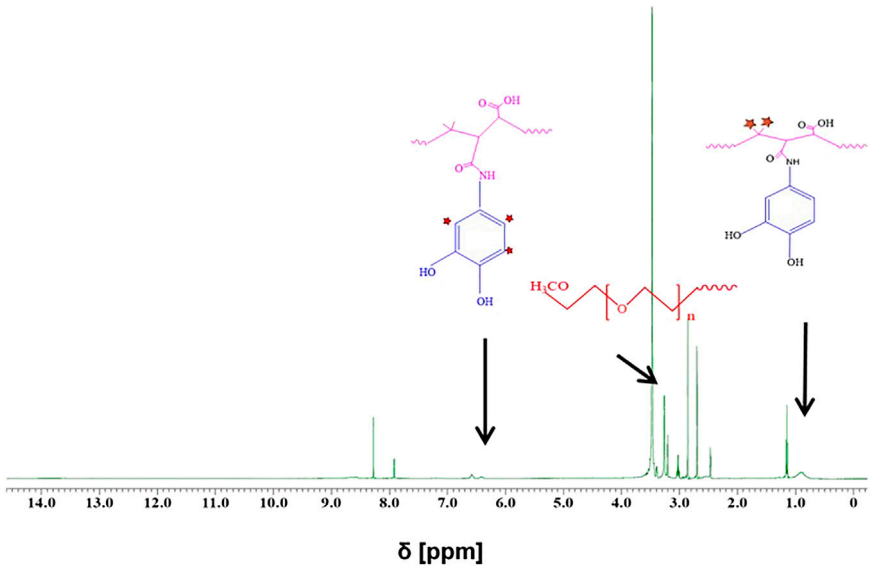

FIGURE 3 | H-NMR spectra of dopamine–PMA–PEG in DMSO-d6. Multiple peaks at chemical shift δ = 6.32–6.78 ppm and a broad peak at ~ 0.9 ppm are, respectively, ascribed to the aromatic protons of catechol and methyl groups in the PMA backbone. The sharp peak at around 3.3 ppm corresponds to the methoxy groups of PEG (H_2N–PEG–OMe).

in aqueous media. The IONPs were hereby coated with polymers, either maintaining or replacing the original ligand shell. An overview of the synthesis strategy is illustrated in **Figure 1**. PMA was selected as a model polymer. Maleic anhydride groups are highly reactive and can be modified with amine containing functional molecules. This nucleophilic addition was carried out without needing any additional reagents, which simplifies the purification steps and characterization of the prepared product (Wang et al., 2015). For polymer coating involving replacement of the original ligands, the polymer was modified with dopamine (Wang et al., 2014). The ligands of dopamine–PMA–PEG were characterized by H-NMR spectroscopy. The presence of methoxy groups, PEG moieties, and catechol groups in the modified PMA was confirmed by H-NMR analysis. A multiple peak at 6.32–6.78 ppm, a sharp peak at around 3.3 ppm, and a broad peak at 0.9 ppm are attributed to the catechol protons of dopamine, PEG, and the methyl group of the modified PMA, respectively (**Figure 3**).

All IONPs were transferred from organic solvent to aqueous solution by polymer coating. **Figure 4** shows negative staining TEM images for IONPs of core diameter d_c = 18 nm. Upon negative staining, apart from the NP coating, also the organic surface coating is visualized. As it can be seen, IONPs coated with PMA–DDA and dopamine–PMA–PEG had core-shell diameters of d_{cs} = 29.65 ± 1.35 and d_{cs} = 29.85 ± 1.28 nm, respectively, confirming the presence of the polymeric shell surrounding each IONP. Based on the negative staining TEM images, both polymer coating techniques of IONPs with 18 nm core size show a mean diameter around d_{cs} = 30 nm.

The hydrodynamic diameters (d_h) of the different IONPs with d_c = 18 nm were determined with DLS. The "hydro"dynamic diameter of the initial IONPs before the polymer coating was determined to be d_h = 24.06 nm in toluene. The corresponding hydrodynamic diameters after the polymer coating were d_h = of 28.97 nm and 30.80 nm for the PMA–DDA and dopamine–PMA–PEG-coated IONPs; see **Table 1**. The DLS data indicate that after the polymer coating, the IONPs had maintained their uniform size with a low polydispersity index (**Table 1**). A negative zeta potential of around ζ = -38.4 and -12.6 mV was determined in water for the PMA–DDA and dopamine–PMA–PEG-coated IONPs, respectively, using laser Doppler anemometry (Hühn et al., 2016).

The PMA–DDA polymer-coated IONPs were also investigated with agarose gel electrophoresis (**Figure 5**). Here, the electrophoretic mobility of the IONPs with different core diameters d_c was investigated. As these IONPs have the same surface chemistry, retardation in electrophoretic mobility is associated with increased diameter, which can be seen in **Figure 5** (Pellegrino et al., 2007). The narrow bands on the polymer-coated IONPs on the gel show that these NPs have homogenous size and charge distribution (Pellegrino et al., 2004). Gel electrophoresis is an excellent method to probe colloidal stability of IONPs (Pellegrino et al., 2007). The buffer has high ionic strength, and by the applied electric field, the IONPs are pulled through the pores of the agarose gel, which removes loosely bound ligands and thus leads to agglomeration. The data shown in **Figure 5** clearly indicate high colloidal stability of the polymer-coated IONPs. Due to their low charge (i.e., zeta potential), the dopamine–PMA-PEG-coated IONPs were not probed by gel electrophoresis.

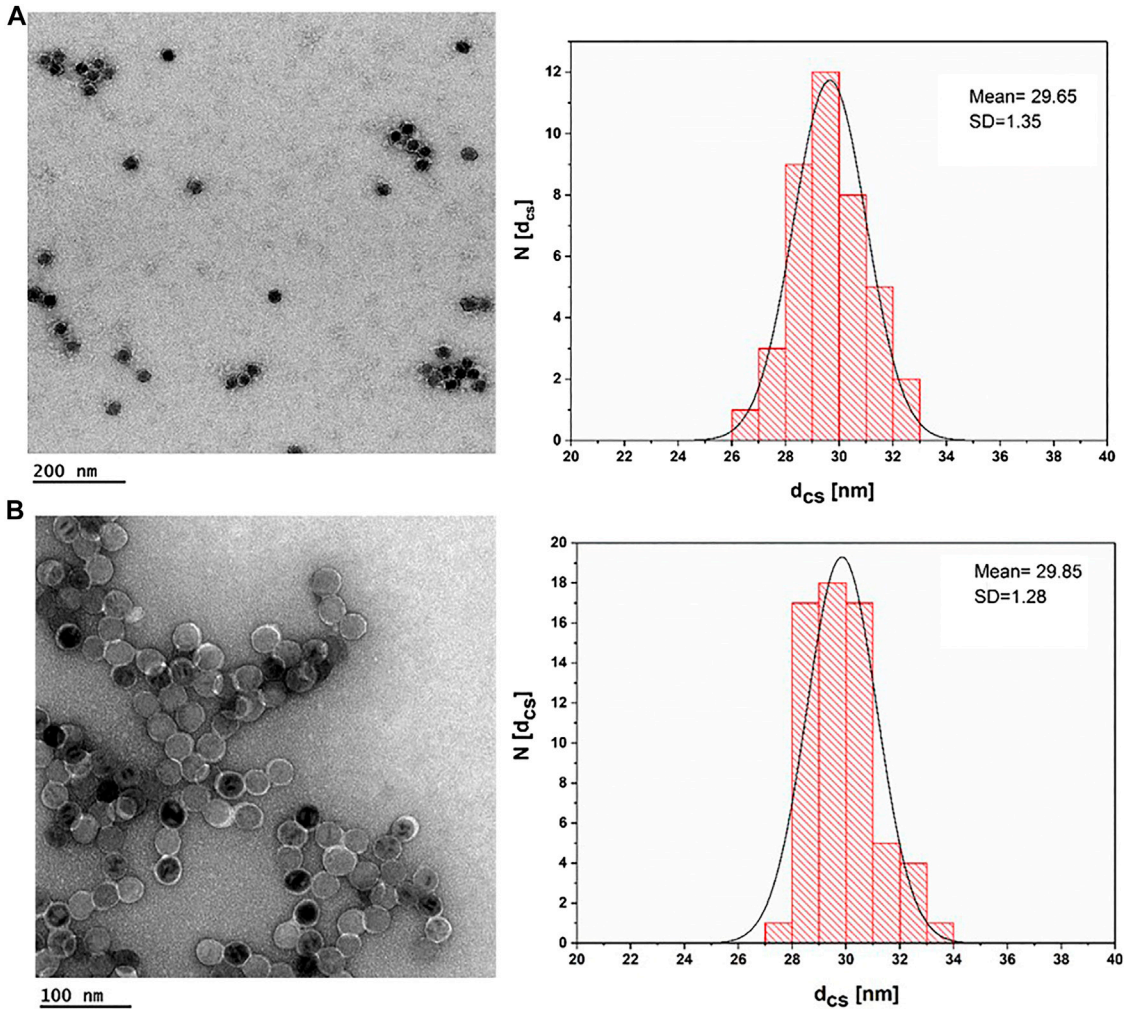

FIGURE 4 | TEM images of IONPs after negative staining with uranyl acetate. **(A)** IONP cores (d_c = 17.6 ± 0.91) plus an organic shell of PMA–DDA, resulting in d_{cs} = 29.65 ± 1.35; the scale bar corresponds to 200 nm. **(B)** IONP cores (d_c = 17.6 ± 0.91) plus an organic shell of dopamine–PMA–PEG, which resulted in d_{cs} = 29.85 ± 1.28; the scale bar is 100 nm.

TABLE 1 | The hydrodynamic diameter d_h of 18 nm IONPs as measured by DLS before and after polymer coating. Values were obtained from the intensity distribution ($d_{h,I}$), the number distribution ($d_{h,N}$), and the Z-average ($d_{h,Z}$). PDI refers to the polydispersity index. Also the mean value of the zeta potential ζ is provided.

Sample	Solvent	$d_{h,I}$ [nm]	$d_{h,N}$ [nm]	$d_{h,Z}$ [nm]	PDI	ζ [mV]
IONP	Toluene	31.15	24.06	29.91	0.01	—
IONP@PMA–DDA	Water	38.69	28.97	36.77	0.29	−38.4
IONP@dopamine–PMA–PEG	Water	59.22	30.80	59.74	0.22	−12.6

Colloidal Stability in Physiological Environments

In various biological applications, NPs are expected to be exposed to salt- and protein-containing media (Pfeiffer et al., 2014). We thus examined the colloidal stability of aqueous dispersions of PMA–DDA and dopamine–PMA–PEG-coated IONPs in sodium chloride and bovine serum albumin (BSA) containing media. Measurements of the effective hydrodynamic diameter were used as a tool to probe the colloidal stability of IONPs (Hühn et al., 2016). Loss in colloidal stability hereby is indicated by agglomeration and thus increased effective hydrodynamic diameters. As aggregation is time dependent, the hydrodynamic diameter of IONPs was measured immediately after exposing the IONPs to NaCl/BSA, and then measurements were repeated after 24 h incubation time at room temperature. DLS histograms of the hydrodynamic

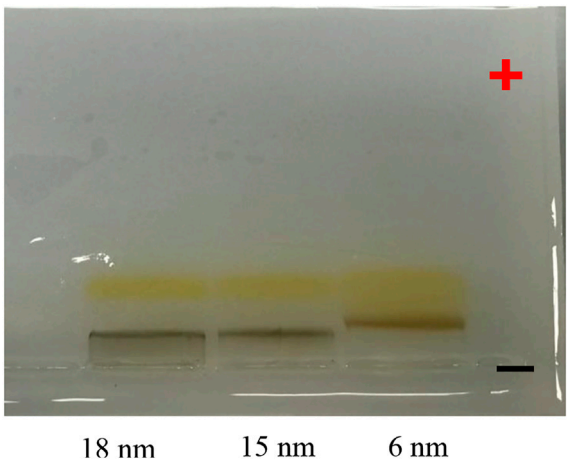

FIGURE 5 | Photographs of an agarose gel on which PMA–DDA-coated IONPs of d_c = 6, 15, and 18 nm had been run for 1 h at 100 V. For this, the IONP samples had first been mixed with Orang-G-containing loading buffer, before they had been loaded into a 2% agarose gel. After the application of voltage, the negatively charged NPs run toward the positive pole.

diameters upon exposure to NaCl/BSA are shown in **Figure 6**. As colloidal stability of the polymer-coated IONPs was already demonstrated with gel electrophoresis (**Figure 5**), here the DLS studies are limited to the bigger IONPs of d_c = 18 nm, as bigger IONPs are more sensitive to agglomeration in general than smaller IONPs. Salt (here in the form of NaCl) in the solution screens the electric charge on the surface of the NPs, thus decreasing the effective surface charge density, resulting in colloidal instability and aggregation of the NPs, as can be seen for the PMA–DDA-coated IONPs. As PEG can contribute steric stabilization, the dopamine–PMA–PEG-coated IONPs are less affected by the addition of salt, which is in good agreement with previous studies (Caballero-Díaz et al., 2013). To probe protein adsorption (Vilanova et al., 2016) on the surface of the polymer-coated IONPs, we used serum albumin (bovine: BSA) as a model protein, because serum albumin is the most abundant protein in blood serum (Hühn et al., 2013). While the protein corona depends on the details of the surface chemistry (Guerrini et al., 2018), here we wanted to probe only colloidal stability. The data of **Figure 6** demonstrate that up to high BSA concentrations, there was no protein-induced agglomeration of the IONPs (apart from the PMA–DDA-coated IONPs at the maximum concentration). Due to limits in the resolution of measuring the hydrodynamic diameter of the NPs with DLS, the formation of the protein corona could not be observed as possible with other techniques (Carril et al., 2017), but the data indicate that, in particular, the dopamine–PMA–PEG-coated IONPs are colloidally stable under physiological conditions.

Relaxivity Measurements

To investigate the MR performance of the polymer-coated IONPs, we carried out longitude relaxivity (r_1) and transverse relaxivity (r_2) measurements. Relaxation times T_i and relaxivities r_i are related by

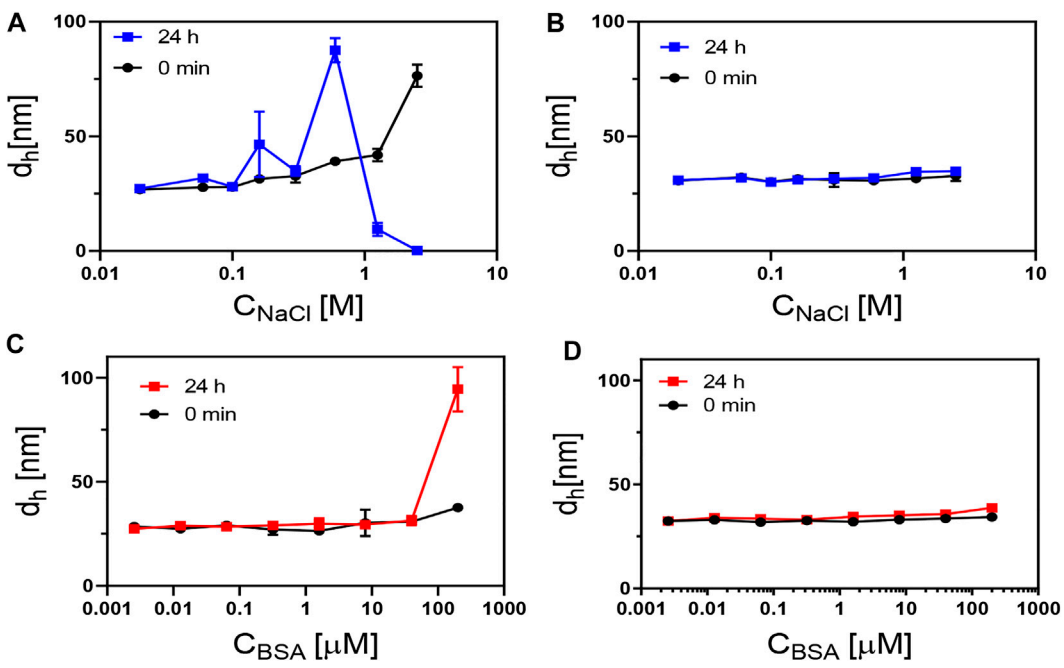

FIGURE 6 | Hydrodynamic diameter (d_h; here, the number distribution $d_{h,N}$ is plotted) of 18 nm IONPs coated with **(A,C)** PMA–DDA and **(B,D)** with dopamine–PMA–PEG, as measured at different concentrations of NaCl and BSA at 0 and 24 h after exposure. In **(A)**, the decrease in d_h at high NaCl concentrations at 24 h is due to sedimentation of the NPs, which, in this way, are no longer in the light path of the DLS measurement.

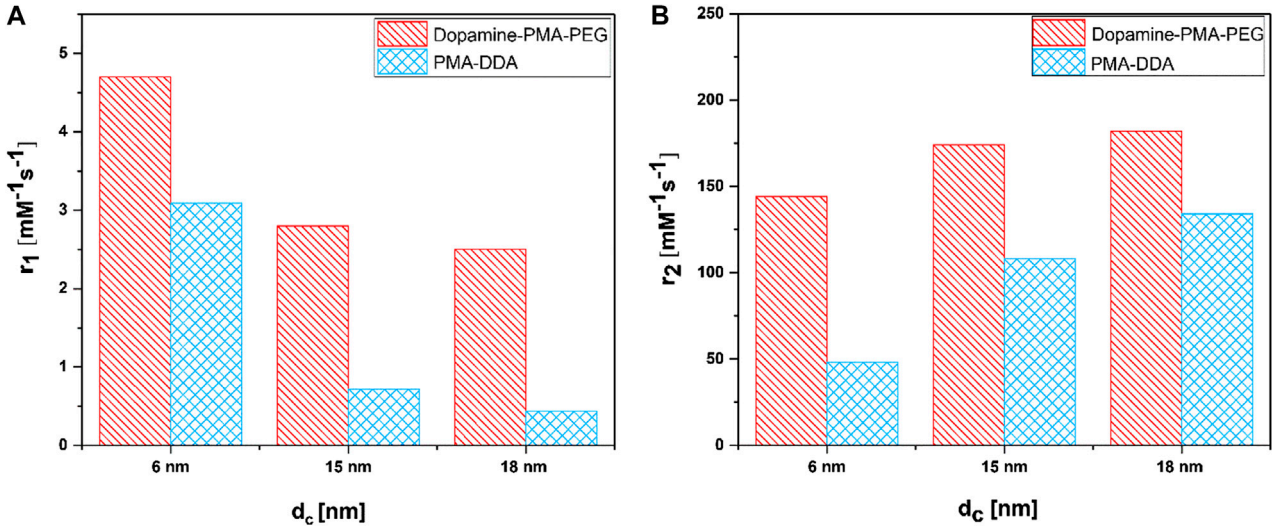

FIGURE 7 | (A) Longitudinal relaxivity (r_1) and **(B)** transverse relaxivity (r_2) as a function of polymer coating and particle size d_c of IONPs.

$$\frac{1}{T_i} = \frac{1}{T_{i,0}} + r_i \cdot C_{Fe}, \tag{2}$$

where T_i are the observed relaxation times in the presence of the contrast agent, $T_{i,0}$ is the relaxation time of pure water protons, and c_{Fe} is the concentration of the MRI contrast agent, in this case, iron (Banerjee et al., 2017). The small IONPs significantly affect the spin–lattice (T_1) relaxation due to the high number of metal ions on the surface and the spins canting, while the spin–spin (T_2) relaxation is related to proton dephasing by local field inhomogeneity (Ni et al., 2017). The data clearly show a dependence of proton relaxivity on particle size (**Figure 7**). This size dependence is believed to arise from surface spin anisotropy, due to the larger surface area–to–volume ratio for smaller IONPs (Smolensky et al., 2013). Since the larger IONPs have more effective magnetic relaxation of the water protons around the NPs, they show higher transverse relaxivity r_2. In addition to the intrinsic material and size-dependent properties of IONPs, the surface coating is also an important factor for T_2 relaxivity (Ni et al., 2017). According to the quantum mechanical outer-sphere theory, the T_2 relaxivity is described by

$$\frac{1}{T_2} = \left(256 \cdot \pi^2 \cdot \frac{\gamma^2}{405}\right) \cdot V^* \cdot \frac{Ms^2 \cdot r^2}{\left[D \cdot \left(1 + \frac{L}{r}\right)\right]}, \tag{3}$$

where V^* and Ms are the volume fraction and the magnetic saturation of the magnetic NPs, respectively, γ is the proton gyromagnetic ratio, r is the radius of the nanoparticles, D is the diffusion coefficient of water, and L is the thickness of an impermeable surface shell on the iron oxide core (Ni et al., 2017). From our experimental data, we can determine $r = d_c/2$ and $L = (d_{cs} - d_c)/2$. The dependence of r_2 from d_c (i.e., r) follows the tendency as given by the formula above: the higher dc, the higher r_2.

The dependence from the surface is harder to discuss, in particular, as it is not known to what degree the polymer shells are impermeable to water. The hydrophilic coating on the surface of the IONPs improves their diffusion and should also partly hinder water molecules to reach the surface of the cores, resulting in faster T_2 relaxation (Zhang et al., 2018). The relaxivity results in **Figure 7** show that dopamine–PMA–PEG-coated IONPs have higher r_2 relaxivity than PMA–DDA-coated IONPs with similar iron oxide core sizes d_c. As mentioned before, at the core size of d_c = 18 nm, the TEM images show no significant difference between the diameters d_cs of IONPs coated with dopamine–PMA–PEG and PMA–DDA. These results indicate that the increase in T_2 relaxivity can be attributed to the increased volume of diffusion of water surrounding each NP to the outer sphere due to the highly hydrophilic nature of PEG in the dopamine–PMA–PEG coating (Duan et al., 2008; Zhang et al., 2018). On the other hand, the catechol groups of dopamine are rich in π-electrons which influence the magnetic field inhomogeneity around the polymer-coated IONPs and accelerate the r_2 relaxivity of water molecules (Zeng et al., 2014).

When IONPs are smaller than d_c = 10 nm, they show dual T_1/T_2 imaging, in which T_1 enhancement refers to surface effects on the magnetization and water/ion metal center interaction on the surface of NPs (Bao et al., 2018; Thapa et al., 2018). According to the inner-outer sphere theory, the exposure of surface iron ions contributes to the T_1 behavior of small IONPs. T_1 relaxation of IONPs arises from direct contact of water protons with the iron (Bao et al., 2018). Therefore, the T_1 signal is very sensitive to surface-capping molecules and their packing density on the surface of the IONPs. Both the exposure of iron ion centers on the surface of NPs and the water accessibility affects the T_1 performance of IONPs (Peng et al., 2016; Bao et al., 2018; Xiao et al., 2018).

Our results reveal that, at similar core sizes d_c, the r_1 relaxivity of polymer-coated IONPs is dependent on the nature of polymer coating (**Figure 7**). In particular, the small IONPs (d_c = 6 nm) coated with dopamine–PMA–PEG show higher r_1 relaxivity than the ones coated with PMA–DDA (**Table 2**). Dopamine serves as a strong anchor

TABLE 2 | Proton relaxivities r_1 and r_2 for IONPs with core sizes of d_c = 6, 15, and 18 nm and two different polymer coatings, as measured at 3 T in water.

Coating	d_c [nm]	r_1 ($mM^{-1}s^{-1}$)	r_2 ($mM^{-1}s^{-1}$)	r_2/r_1
PMA–DDA	6	3.09	48.3	15.63
PMA–DDA	15	0.72	108	150
PMA–DDA	18	0.44	135	306.8
Dopamine–PMA–PEG	6	4.7	144	30.64
Dopamine–PMA–PEG	15	2.8	174.9	62.46
Dopamine–PMA–PEG	18	2.4	183	76.25
Gd-DOTA	—	2.72	3.1	1.14

group to functionalize IONPs. Indeed, the catechol unit in dopamine exhibits a specific affinity to the surface of IONPs, as a result of improved orbital overlap of the five-membered catechol ring and reduced steric effect (Chi et al., 2013; Palui et al., 2015). In dopamine–PMA–PEG-coated IONPs, the catechol groups of dopamine are replaced with oleic acid as the original hydrophobic ligand on the surface of IONPs and provide hydrophilic dispersion of the NPs. On the other hand, the IONPs can be encapsulated by amphiphilic PMA–DDA, in which the hydrophobic oleic acid is wrapped within the polymer layer. Encapsulation of the IONPs is carried out by hydrophobic interaction between oleic acid and the dodecylamine groups (Lin et al., 2008). This hydrophobic layer restricts the access of water protons to the surface of the magnetic NPs. Hence, IONPs coated with dopamine–PMA–PEG show higher r_1 relaxivity than IONPs coated with PMA–DDA. The r_1 relaxivity of dopamine–PMA–PEG is also higher than the one of Gd-DOTA (Dotarem®) as a positive contrast agent with 2.7 $mM^{-1}s^{-1}$ at 3 T. We note that we focused on our discussion about comparing of r_1 and r_2. However, there are also other contrast modalities. For example, contrast is often discussed in terms of r_2/r_1 (Lee, 2011). The respective values for the here investigated IONPs are enlisted in **Table 2**.

CONCLUSION

In summary, IONPs of 6, 15, and 18 nm core diameter with a narrow size distribution were synthesized through thermal decomposition, followed by polymer coating with/without replacement of the original ligand shell. Polymer coating of IONPs with dopamine–PMA–PEG exhibited higher colloidal stability in NaCl-containing solutions. Furthermore, proton relaxivity measurements demonstrated high r_1 and r_2 relaxivities for 6 and 18 nm dopamine–PMA–PEG-coated IONPs, respectively. Considering the higher colloidal stability and enhancement of negative and positive contrast of dopamine–PMA–PEG-coated IONPs with increase in size, this polymer could be assumed as an efficient candidate for polymer coating of IONPs as T_1 and T_2 contrast agents. Thereupon, the present investigation of r_1 and r_2 relaxivities of IONPs with different surface coatings and similar shell sizes helps toward a reasonable understanding of surface impacts in obtaining high-performance NPs as MRI contrast agents. While here the focus is given on the aspect of the influence of the surface coating on relaxivity, future studies would also have to take into account other effects of the surface coating, such as different biocompatibilities and biodistributions.

DATA AVAILABILITY STATEMENT

The original contributions presented in the study are included in the article/**Supplementary Material**; further inquiries can be directed to the corresponding author.

AUTHOR CONTRIBUTIONS

Conceptualization: FA, NF, and WP; formal analysis: FA; funding acquisition: WP; investigation: FA and AM; resources: WP and SS; supervision: NF; writing original draft: FA; reviewing and editing: FA, AM, NF, WP, and SS.

ACKNOWLEDGMENTS

Parts of this work were funded by the Cluster of Excellence "Advanced Imaging of Matter" of the Deutsche Forschungsgemeinschaft (DFG), EXC 2056-project ID 390715994. FA and SS also would like to acknowledge financial support provided by the Tarbiat Modares University and Iran Science Elite Federation.

SUPPLEMENTARY MATERIAL

The Supplementary Material for this article can be found online at: https://www.frontiersin.org/articles/10.3389/fnano.2021.644734/full#supplementary-material.

REFERENCES

Ahmad, T., Rhee, I., Hong, S., Chang, Y., and Lee, J. (2011). Ni-Fe_2O_4 nanoparticles as contrast agents for magnetic resonance imaging. *J. Nanosci. Nanotechnol.* 11 (7), 5645–5650. doi:10.1166/jnn.2011.4502

Ahmadpoor, F., Delavari, H., and Shojaosadati, S. A. (2020). Porous versus dense—effect of silica coating on contrast enhancement of iron carbide nanoparticles in T_2 -weighted magnetic resonance imaging. *ChemistrySelect* 5 (3), 1135–1139. doi:10.1002/slct.201902548

Ali, A., Zafar, H., Zia, M., Ul Haq, I., Phull, A. R., Ali, J. S., et al. (2016). Synthesis, characterization, applications, and challenges of iron oxide nanoparticles. *Nanotechnol. Sci. Appl.* 9, 49. doi:10.2147/NSA.S99986

Banerjee, A., Blasiak, B., Pasquier, E., Tomanek, B., and Trudel, S. (2017). Synthesis, characterization, and evaluation of PEGylated first-row transition metal ferrite nanoparticles as T2contrast agents for high-field MRI. *RSC Adv.* 7 (61), 38125–38134. doi:10.1039/c7ra05495e

Bao, Y., Sherwood, J. A., and Sun, Z. (2018). Magnetic iron oxide nanoparticles as T_1 contrast agents for magnetic resonance imaging. *J. Mater. Chem. C* 6 (6), 1280–1290. doi:10.1039/c7tc05854c

Bauer, L. M., Situ, S. F., Griswold, M. A., and Samia, A. C. (2015). Magnetic particle imaging tracers: state-of-the-art and future directions. *J. Phys. Chem. Lett.* 6 (13), 2509–2517. doi:10.1021/acs.jpclett.5b00610

Bruns, O. T., Ittrich, H., Peldschus, K., Kaul, M. G., Tromsdorf, U. I., Lauterwasser, J., et al. (2009). Real-time magnetic resonance imaging and quantification of lipoprotein metabolism *in vivo* using nanocrystals. *Nat. Nanotechnol.* 4 (3), 193. doi:10.1038/nnano.2008.405

Caballero-Díaz, E., Pfeiffer, C., Kastl, L., Rivera-Gil, P., Simonet, B., Valcárcel, M., et al. (2013). The toxicity of silver nanoparticles depends on their uptake by cells and thus on their surface chemistry. *Part. Part. Syst. Char.* 30 (12), 1079–1085. doi:10.1002/ppsc.201300215

Carril, M., Padro, D., del Pino, P., Carrillo-Carrion, C., Gallego, M., and Parak, W. J. (2017). *In situ* detection of the protein Corona in complex environments. *Nat. Commun.* 8 (1), 1542. doi:10.1038/s41467-017-01826-4

Chi, X., Wang, X., Hu, J., Wang, L., Gao, J., Zhang, B., et al. (2013). Dopamine serves as a stable surface modifier for iron oxide nanoparticles. *J. Mol. Eng. Mater.* 1 (02), 1350001. doi:10.1142/s2251237313500019

Corrias, A., Mountjoy, G., Loche, D., Puntes, V., Falqui, A., Zanella, M., et al. (2009). Identifying spinel phases in nearly monodisperse iron oxide colloidal nanocrystal. *J. Phys. Chem. C* 113 (43), 18667–18675. doi:10.1021/jp9047677

Duan, H., Kuang, M., Wang, X., Wang, Y. A., Mao, H., and Nie, S. (2008). Reexamining the effects of particle size and surface chemistry on the magnetic properties of iron oxide nanocrystals: new insights into spin disorder and proton relaxivity. *J. Phys. Chem. C* 112 (22), 8127–8131. doi:10.1021/jp8029083

Feng, Q., Liu, Y., Huang, J., Chen, K., Huang, J., and Xiao, K. (2018). Uptake, distribution, clearance, and toxicity of iron oxide nanoparticles with different sizes and coatings. *Sci. Rep.* 8 (1), 1–13. doi:10.1038/s41598-018-19628-z

Fernández-Argüelles, M. T., Yakovlev, A., Sperling, R. A., Luccardini, C., Gaillard, S., Sanz Medel, A., et al. (2007). Synthesis and characterization of polymer-coated quantum dots with integrated acceptor dyes as FRET-based nanoprobes. *Nano Lett.* 7 (9), 2613–2617. doi:10.1021/nl070971d

Fernández-Barahona, I., Muñoz-Hernando, M., Ruiz-Cabello, J., Herranz, F., and Pellico, J. (2020). Iron oxide nanoparticles: an alternative for positive contrast in magnetic resonance imaging. *Inorganics* 8 (4), 28. doi:10.3390/inorganics8040028

Guerrini, L., Alvarez-Puebla, R., and Pazos-Perez, N. (2018). Surface modifications of nanoparticles for stability in biological fluids. *Materials* 11 (7), 1154. doi:10.3390/ma11071154

Heine, M., Bartelt, A., Bruns, O. T., Bargheer, D., Giemsa, A., Freund, B., et al. (2014). The cell-type specific uptake of polymer-coated or micelle-embedded QDs and SPIOs does not provoke an acute pro-inflammatory response in the liver. *Beilstein J. Nanotechnol.* 5 (1), 1432–1440. doi:10.3762/bjnano.5.155

Hobson, N. J., Weng, X., Siow, B., Veiga, C., Ashford, M., Thanh, N. T., et al. (2019). Clustering superparamagnetic iron oxide nanoparticles produces organ-targeted high-contrast magnetic resonance images. *Nanomedicine* 14 (9), 1135–1152. doi:10.2217/nnm-2018-0370

Huang, J., Zhong, X., Wang, L., Yang, L., and Mao, H. (2012). Improving the magnetic resonance imaging contrast and detection methods with engineered magnetic nanoparticles. *Theranostics* 2 (1), 86. doi:10.7150/thno.4006

Hühn, D., Kantner, K., Geidel, C., Brandholt, S., De Cock, I., Soenen, S. J., et al. (2013). Polymer-coated nanoparticles interacting with proteins and cells: focusing on the sign of the net charge. *ACS Nano* 7 (4), 3253–3263.

Hühn, J., Carrillo-Carrion, C., Soliman, M. G., Pfeiffer, C., Valdeperez, D., Masood, A., et al. (2016). Selected standard protocols for the synthesis, phase transfer, and characterization of inorganic colloidal nanoparticles. *Chem. Mater.* 29 (1), 399–461. doi:10.1021/acs.chemmater.6b04738

Joris, F., Valdepérez, D., Pelaz, B., Wang, T., Doak, S. H., Manshian, B. B., et al. (2017). Choose your cell model wisely: the *in vitro* nanoneurotoxicity of differentially coated iron oxide nanoparticles for neural cell labeling. *Acta Biomater.* 55, 204–213. doi:10.1016/j.actbio.2017.03.053

Jun, Y. W., Seo, J. W., and Cheon, J. (2008). Nanoscaling laws of magnetic nanoparticles and their applicabilities in biomedical sciences. *Acc. Chem. Res.* 41 (2), 179–189. doi:10.1021/ar700121f

Karimi, M., Ghasemi, A., Sahandi Zangabad, P., Rahighi, R., Moosavi Basri, S. M., Mirshekari, H., et al. (2016). Smart micro/nanoparticles in stimulus-responsive drug/gene delivery systems. *Chem. Soc. Rev.* 45 (5), 1457–1501. doi:10.1039/c5cs00798d

Khawaja, A. Z., Cassidy, D. B., Al Shakarchi, J., McGrogan, D. G., Inston, N. G., and Jones, R. G. (2015). Revisiting the risks of MRI with gadolinium based contrast agents-review of literature and guidelines. *Insights into imaging* 6 (5), 553–558. doi:10.1007/s13244-015-0420-2

Komadel, P., and Stucki, J. W. (1988). Quantitative assay of minerals for Fe^{2+} and Fe^{3+} using 1,10-phenanthroline III: a rapid photochemical method. *Clays Clay Miner.* 36 (4), 379–381. doi:10.1346/ccmn.1988.0360415

Kudr, J., Haddad, Y., Richtera, L., Heger, Z., Cernak, M., Adam, V., et al. (2017). Magnetic nanoparticles: from design and synthesis to real world applications. *Nanomaterials* 7 (9), 243. doi:10.3390/nano7090243

Kurzhals, S., Schroffenegger, M., Gal, N., Zirbs, R., and Reimhult, E. (2017). Influence of grafted block copolymer structure on thermoresponsiveness of superparamagnetic core-shell nanoparticles. *Biomacromolecules* 19 (5), 1435–1444. doi:10.1021/acs.biomac.7b01403

Kwon, H. J., Shin, K., Soh, M., Chang, H., Kim, J., Lee, J., et al. (2018). Large-scale synthesis and medical applications of uniform-sized metal oxide nanoparticles. *Adv. Mater.* 30 (42), 1704290. doi:10.1002/adma.201704290

Laurent, S., Dutz, S., Häfeli, U. O., and Mahmoudi, M. (2011). Magnetic fluid hyperthermia: focus on superparamagnetic iron oxide nanoparticles. *Adv. Colloid Interface Sci.* 166 (1–2), 8–23. doi:10.1016/j.cis.2011.04.003

Lee, D. Y. (2011). Highly effective T2 MR contrast agent based on heparinized superparamagnetic iron oxide nanoparticles. *Macromol. Res.* 19 (8), 843–847. doi:10.1007/s13233-011-0805-0

Lee, N., and Hyeon, T. (2012). Designed synthesis of uniformly sized iron oxide nanoparticles for efficient magnetic resonance imaging contrast agents. *Chem. Soc. Rev.* 41 (7), 2575–2589. doi:10.1039/c1cs15248c

Li, D., Jiang, D., Chen, M., Xie, J., Wu, Y., Dang, S., et al. (2010). An easy fabrication of monodisperse oleic acid-coated Fe_3O_4 nanoparticles. *Mater. Lett.* 64 (22), 2462–2464. doi:10.1016/j.matlet.2010.08.025

Li, F., Liang, Z., Liu, J., Sun, J., Hu, X., Zhao, M., et al. (2019). Dynamically reversible iron oxide nanoparticle assemblies for targeted amplification of T_1-weighted magnetic resonance imaging of tumors. *Nano Lett.* 19 (7), 4213–4220. doi:10.1021/acs.nanolett.8b04411

Li, Q., Kartikowati, C. W., Horie, S., Ogi, T., Iwaki, T., and Okuyama, K. (2017). Correlation between particle size/domain structure and magnetic properties of highly crystalline Fe_3O_4 nanoparticles. *Sci. Rep.* 7 (1), 9894. doi:10.1038/s41598-017-09897-5

Lin, C. A., Sperling, R. A., Li, J. K., Yang, T. Y., Li, P. Y., Zanella, M., et al. (2008). Design of an amphiphilic polymer for nanoparticle coating and functionalization. *Small* 4 (3), 334–341. doi:10.1002/smll.200700654

McDonald, R. J., McDonald, J. S., Kallmes, D. F., Jentoft, M. E., Murray, D. L., Thielen, K. R., et al. (2015). Intracranial gadolinium deposition after contrast-enhanced MR imaging. *Radiology* 275 (3), 772–782. doi:10.1148/radiol.15150025

Morales, M. P., Serna, C. J., Bødker, F., and Mørup, S. (1997). Spin canting due to structural disorder in maghemite. *J. Phys. Condens. Matter* 9 (25), 5461. doi:10.1088/0953-8984/9/25/013

Muthukumaran, T., and Philip, J. (2016). Effect of phosphate and oleic acid capping on structure, magnetic properties and thermal stability of iron oxide nanoparticles. *J. Alloys Compd.* 689, 959–968. doi:10.1016/j.jallcom.2016.08.067

Ni, D., Bu, W., Ehlerding, E. B., Cai, W., and Shi, J. (2017). Engineering of inorganic nanoparticles as magnetic resonance imaging contrast agents. *Chem. Soc. Rev.* 46 (23), 7438–7468. doi:10.1039/c7cs00316a

Palui, G., Aldeek, F., Wang, W., and Mattoussi, H. (2015). Strategies for interfacing inorganic nanocrystals with biological systems based on polymer-coating. *Chem. Soc. Rev.* 44 (1), 193–227. doi:10.1039/c4cs00124a

Pardo, A., Pelaz, B., Gallo, J., Bañobre-López, M., Parak, W. J., Barbosa, S., et al. (2020). Synthesis, characterization, and evaluation of superparamagnetic doped ferrites as potential therapeutic nanotools. *Chem. Mater.* 32 (6), 2220–2231. doi:10.1021/acs.chemmater.9b04848

Park, J., An, K., Hwang, Y., Park, J. G., Noh, H. J., Kim, J. Y., et al. (2004). Ultra-large-scale syntheses of monodisperse nanocrystals. *Nat. Mater.* 3 (12), 891. doi:10.1038/nmat1251

Patil, R. M., Thorat, N. D., Shete, P. B., Bedge, P. A., Gavde, S., Joshi, M. G., et al. (2018). Comprehensive cytotoxicity studies of superparamagnetic iron oxide nanoparticles. *Biochem. Biophys. Rep.* 13, 63–72. doi:10.1016/j.bbrep.2017.12.002

Patsula, V., Horák, D., Kučka, J., Macková, H., Lobaz, V., Francová, P., et al. (2019). Synthesis and modification of uniform PEG-neridronate-modified magnetic nanoparticles determines prolonged blood circulation and biodistribution in a mouse preclinical model. *Sci. Rep.* 9 (1), 10765. doi:10.1038/s41598-019-47262-w

Pellegrino, T., Manna, L., Kudera, S., Liedl, T., Koktysh, D., Rogach, A. L., et al. (2004). Hydrophobic nanocrystals coated with an amphiphilic polymer shell: a general route to water soluble nanocrystals. *Nano Lett.* 4 (4), 703–707. doi:10.1021/nl035172j

Pellegrino, T., Sperling, R. A., Alivisatos, A. P., and Parak, W. J. (2007). Gel electrophoresis of gold-DNA nanoconjugates. *J. Biomed. Biotechnol.* 2007, 26796. doi:10.1155/2007/26796

Peng, Y.-K., Tsang, S. C. E., and Chou, P.-T. (2016). Chemical design of nanoprobes for T1-weighted magnetic resonance imaging. *Mater. Today* 19 (6), 336–348. doi:10.1016/j.mattod.2015.11.006

Pfeiffer, C., Rehbock, C., Hühn, D., Carrillo-Carrion, C., de Aberasturi, D. J., Merk, V., et al. (2014). Interaction of colloidal nanoparticles with their local environment: the (ionic) nanoenvironment around nanoparticles is different from bulk and determines the physico-chemical properties of the nanoparticles. *J. R. Soc. Interface* 11 (96), 20130931. doi:10.1098/rsif.2013.0931

Sheel, R., Kumari, P., Panda, P. K., Jawed Ansari, M. D., Patel, P., Singh, S., et al. (2020). Molecular intrinsic proximal interaction infer oxidative stress and apoptosis modulated *in vivo* biocompatibility of P. *niruri* contrived antibacterial iron oxide nanoparticles with zebrafish. *Environ. Pollut.* 267, 115482. doi:10.1016/j.envpol.2020.115482

Shen, Z., Chen, T., Ma, X., Ren, W., Zhou, Z., Zhu, G., et al. (2017). Multifunctional theranostic nanoparticles based on exceedingly small magnetic iron oxide nanoparticles for T1-weighted magnetic resonance imaging and chemotherapy. *ACS Nano* 11 (11), 10992–11004. doi:10.1021/acsnano.7b04924

Smith, B. R., and Gambhir, S. S. (2017). Nanomaterials for *in vivo* imaging. *Chem. Rev.* 117 (3), 901–986. doi:10.1021/acs.chemrev.6b00073

Smolensky, E. D., Park, H. Y., Zhou, Y., Rolla, G. A., Marjańska, M., Botta, M., et al. (2013). Scaling laws at the nano size: the effect of particle size and shape on the magnetism and relaxivity of iron oxide nanoparticle contrast agents. *J. Mater. Chem. B* 1 (22), 2818–2828. doi:10.1039/C3TB00369H

Sun, S., Zeng, H., Robinson, D. B., Raoux, S., Rice, P. M., Wang, S. X., et al. (2004). Monodisperse MFe_2O_4 (M = Fe, Co, Mn) nanoparticles. *J. Am. Chem. Soc.* 126 (1), 273–279. doi:10.1021/ja0380852

Thapa, B., Diaz-Diestra, D., Santiago-Medina, C., Kumar, N., Tu, K., Beltran-Huarac, J., et al. (2018). T1- and T2-weighted magnetic resonance dual contrast by single core truncated cubic iron oxide nanoparticles with abrupt cellular internalization and immune evasion. *ACS Appl. Bio Mater.* 1 (1), 79–89. doi:10.1021/acsabm.8b00016

Tromsdorf, U. I., Bigall, N. C., Kaul, M. G., Bruns, O. T., Nikolic, M. S., Mollwitz, B., et al. (2007). Size and surface effects on the MRI relaxivity of manganese ferrite nanoparticle contrast agents. *Nano Lett.* 7 (8), 2422–2427. doi:10.1021/nl071099b

Tromsdorf, U. I., Bruns, O. T., Salmen, S. C., Beisiegel, U., and Weller, H. (2009). A highly effective, nontoxic T_1 MR contrast agent based on ultrasmall PEGylated iron oxide nanoparticles. *Nano Lett.* 9 (12), 4434–4440. doi:10.1021/nl902715v

Vakili-Ghartavol, R., Momtazi-Borojeni, A. A., Vakili-Ghartavol, Z., Aiyelabegan, H. T., Jaafari, M. R., Rezayat, S. M., et al. (2020). Toxicity assessment of superparamagnetic iron oxide nanoparticles in different tissues. *Artif. cells Nanomed. Biotechnol.* 48 (1), 443–451. doi:10.1080/21691401.2019.1709855

Vanhecke, D., Kuhn, D. A., Jimenez de Aberasturi, D., Balog, S., Milosevic, A., Urban, D., et al. (2017). Involvement of two uptake mechanisms of gold and iron oxide nanoparticles in a co-exposure scenario using mouse macrophages. *Beilstein J. Nanotechnol.* 8 (1), 2396–2409. doi:10.3762/bjnano.8.239

Vilanova, O., Mittag, J. J., Kelly, P. M., Milani, S., Dawson, K. A., Rädler, J. O., et al. (2016). Understanding the kinetics of protein-nanoparticle corona formation. *ACS Nano* 10 (12), 10842–10850. doi:10.1021/acsnano.6b04858

Wang, L., Huang, J., Chen, H., Wu, H., Xu, Y., Li, Y., et al. (2017). Exerting enhanced permeability and retention effect driven delivery by ultrafine iron oxide nanoparticles with T1-T2 switchable magnetic resonance imaging contrast. *ACS Nano* 11 (5), 4582–4592. doi:10.1021/acsnano.7b00038

Wang, W., Aldeek, F., Ji, X., Zeng, B., and Mattoussi, H. (2015). A multifunctional amphiphilic polymer as a platform for surface-functionalizing metallic and other inorganic nanostructures. *Faraday Discuss.* 175, 137–151. doi:10.1039/c4fd00154k

Wang, W., Ji, X., Na, H. B., Safi, M., Smith, A., Palui, G., et al. (2014). Design of a multi-dopamine–modified polymer ligand optimally suited for interfacing magnetic nanoparticles with biological systems. *Langmuir* 30 (21), 6197–6208. doi:10.1021/la500974r

Wei, H., Bruns, O. T., Kaul, M. G., Hansen, E. C., Barch, M., Wiśniowska, A., et al. (2017). Exceedingly small iron oxide nanoparticles as positive MRI contrast agents. *Proc. Natl. Acad. Sci. U.S.A.* 114 (9), 2325–2330. doi:10.1073/pnas.1620145114

Woodard, L. E., Dennis, C. L., Borchers, J. A., Attaluri, A., Velarde, E., Dawidczyk, C., et al. (2018). Nanoparticle architecture preserves magnetic properties during coating to enable robust multi-modal functionality. *Sci. Rep.* 8 (1), 1–13. doi:10.1038/s41598-018-29711-0

Wu, W., Wu, Z., Yu, T., Jiang, C., and Kim, W. S. (2015). Recent progress on magnetic iron oxide nanoparticles: synthesis, surface functional strategies and biomedical applications. *Sci. Technol. Adv. Mater.* 16 (2), 023501. doi:10.1088/1468-6996/16/2/023501

Xiao, W., Legros, P., Chevallier, P., Lagueux, J., Oh, J. K., and Fortin, M.-A. (2018). Superparamagnetic iron oxide nanoparticles stabilized with multidentate block copolymers for optimal vascular contrast in T1-weighted magnetic resonance imaging. *ACS Appl. Nano Mater.* 1 (2), 894–907. doi:10.1021/acsanm.7b00300

Yang, F., Riedel, R., del Pino, P., Pelaz, B., Said, A. H., Soliman, M., et al. (2017). Real-time, label-free monitoring of cell viability based on cell adhesion measurements with an atomic force microscope. *J. Nanobiotechnol.* 15 (1), 23. doi:10.1186/s12951-017-0256-7

Zeng, J., Jing, L., Hou, Y., Jiao, M., Qiao, R., Jia, Q., et al. (2014). Anchoring group effects of surface ligands on magnetic properties of Fe_3O_4 nanoparticles: towards high performance MRI contrast agents. *Adv. Mater.* 26 (17), 2694–2698. doi:10.1002/adma.201304744

Zhang, W., Liu, L., Chen, H., Hu, K., Delahunty, I., Gao, S., et al. (2018). Surface impact on nanoparticle-based magnetic resonance imaging contrast agents. *Theranostics* 8 (9), 2521. doi:10.7150/thno.23789

Zhao, Z., Zhou, Z., Bao, J., Wang, Z., Hu, J., Chi, X., et al. (2013). Octapod iron oxide nanoparticles as high-performance T_2 contrast agents for magnetic resonance imaging. *Nat. Commun.* 4 (1), 2266–2267. doi:10.1038/ncomms3266

Zhu, L., Pelaz, B., Chakraborty, I., and Parak, W. (2019). Investigating possible enzymatic degradation on polymer shells around inorganic nanoparticles. *Int. J. Mol. Sci.* 20 (4), 935. doi:10.3390/ijms20040935

Conflict of Interest: The authors declare that the research was conducted in the absence of any commercial or financial relationships that could be construed as a potential conflict of interest.